Highly fluorescent, color tunable and magnetic quaternary Ag–In–Mn–Zn–S quantum dots

Perizat Galiyeva, Halima Alem, Hervé Rinnert, Lavinia Balan, Sébastien Blanchard, Ghouti Medjahdi, Bolat Uralbekov, Raphael Schneider

Highly fluorescent, color tunable and magnetic quaternary Ag-In-Mn-Zn-S quantum dots

Perizat Galiyeva,[a] Halima Alem,[b] Hervé Rinnert,[b] Lavinia Balan,[c] Sébastien Blanchard,[d] Ghouti Medjahdi,[b] Bolat Uralbekov [e] and Raphaël Schneider*[a]

[a.] *Laboratoire Réactions et Génie des Procédés, Université de Lorraine, CNRS, LRGP, F-54000 Nancy, France.*

[b.] *Institut Jean Lamour, Université de Lorraine, CNRS, F-54506 Vandoeuvre-lès-Nancy, France. E-mail:raphael.schneider@univ-lorraine.fr*

[c.] *Institut de Science des Matériaux de Mulhouse (IS2M), CNRS, UMR 7361, 15 rue Jean Starcky, 68093 Mulhouse, France.*

[d.] *Sorbonne Université, CNRS, Institut Parisien de Chimie Moléculaire, IPCM, F-75005 Paris, France*

[e.] *Al-Farabi Kazakh National University, Al-Farabi Av., 71, Almaty 050040, Kazakhstan.*

Electronic Supplementary Information (ESI) available. See DOI: 10.1039/C9QI00131J

Abstract

Mn-doped quantum dots (QDs) are of high interest for numerous applications like solar cells, optoelectronics, optosensing, or bioimaging. Here, we report the preparation of quaternary $(AgInS_2)_x(MnS)_y(ZnS)_{1-x-y}$ QDs, thereafter noted Mn:AIZS via a thermally induced decomposition of Ag, In, Zn and Mn precursors in the presence of oleylamine and dodecanethiol. The Mn:AIZS QDs have an average diameter of 3.5 nm and their XRD patterns can be indexed with the orthorhombic phase of $AgInS_2$. The incorporation of Mn^{2+} ions in the AIZS crystal lattice results in a red-shift of the photoluminescence (PL) emission maximum depending on the Mn^{2+} content. The PL quantum yields decrease upon loading with Mn^{2+} but remained high (53-31%) until 50% theoretical loading in Mn^{2+}. Steady state, PL excitation and time-resolved PL measurements suggest that Mn^{2+}-dependent trap states are involved in the PL emission. Mn:AIZS QDs exhibit also magnetic properties. In addition, Mn:AIZS QDs can easily be transferred to the aqueous phase using the PMAO amphiphilic polymer without alteration of their optical properties (PL quantum yield up to 51%), revealing their high potential for biological applications.

Introduction

In recent years, I-III-VI_2-based semiconductor quantum dots (QDs) like $CuInS_2$ (CIS) or $AgInS_2$ (AIS) and their I-II-III-VI_2 alloys with ZnS (CIZS and AIZS, respectively) have gained high interest as alternatives to binary QDs like CdSe or CdTe because these nanocrystals are composed of weakly toxic elements and their optical properties can be controlled by varying their size and their composition.[1-5] The bandgap of these QDs can be tuned from the visible to the near-infrared spectrum making them suitable for applications like photocatalysis,[6,7] light-emitting diodes,[8,9] solar cells,[10] bio-imaging[11,12] or bio-sensing.[13-15] Although the full-width at half-maximum (fwhm) of the photoluminescence (PL) emission, and thus the color purity, of I-II-III-VI_2 QDs is larger (ca. 100 nm) than that of binary QDs like CdSe, these nanocrystals not only exhibit long PL lifetimes but also large Stokes shift between the absorption and the PL emission and thus do not suffer from self-absorption or non-radiative Förster resonance energy transfer.

For II-VI QDs, the PL emission usually originates from exciton recombination. For I-II-III-VI_2 QDs, the PL emission mechanism is more complex and still under debate.[16-21] Due to their heterogeneous composition, these dots contain high native defect densities which make their electronic band structures difficult to determine. For AIZS QDs, silver vacancies (V_{ag}), sulfur vacancies (V_S), silver interstitial atoms (Ag_{int}) and sulfur interstitial atoms (S_{int}) have been reported and V_S and Ag_{int} behave as donors while V_{Ag} and S_{int} as acceptors.[17,22,23] Therefore, the recombination of carriers trapped by intragap levels originating from surface defects, also called donor-acceptor (D-A) pair recombination, markedly contributes to the PL emission. The PL emission of AIZS QDs was demonstrated to exhibit two components: (1) a fast transition with a PL lifetime of ca 25 ns originating from a delocalized valence/conduction band transition and (2) a slower component (PL lifetime higher than 185 ns) originating from the deep D-A pair transition, its contribution being dependent on the composition of the nanocrystals.[18]

The incorporation of transition metal cations like Mn^{2+} in QDs allows not only to confer to these nanocrystals new properties like magnetism but also to tune their optical properties. To date, the doping of CIZS or AIZS QDs with Mn^{2+} ions has only scarcely been investigated. When using a low amount of Mn^{2+} and a high level of Zn^{2+} ions in CIZS or AIZS QDs, the D-A emission was suppressed and only the PL emission originating from the Mn^{2+} $^4T_1 \rightarrow {}^6A_1$

transition located at ca. 600 nm was observed.[24,25] The temperature-dependent PL properties of Mn-doped CIZS was also demonstrated.[26] When Mn^{2+} were adsorbed at the periphery of the CIS cores followed by the ZnS shell coating and the alloying, the obtained nanocrystals exhibited both the Mn^{2+} and the D-A pair emissions.[27]

In this paper, we report the incorporation of Mn^{2+} ions in green- or orange-emitting AIZS QDs via a one-pot reaction conducted in oleylamine (OAm). The loading in Mn^{2+} was varied from 25 to 75% relative to the total amount of metal cations in the dots to prepare quaternary $(AgInS_2)_x(MnS)_y(ZnS)_{1-x-y}$ QDs, thereafter noted Mn:AIZS. Our results show that the PL emission of Mn:AIZS QDs, originating from the D-A pair recombination, can be tuned by varying the Mn^{2+} content of the dots. Time-resolved PL was used to investigate the PL behaviors of Mn:AIZS QDs at different Mn^{2+} loadings. The small sized, highly fluorescent and magnetic Mn:AIZS QDs can easily be transferred in aqueous solution using poly(maleic anhydride-alt-1-octadecene) (PMAO) and are therefore of high potential for bio-imaging or cells labeling and sorting.

Results and discussion

Morphology and structure characterization

Mn:AIZS QDs were prepared via a one-pot synthetic protocol developed for AIZS QDs,[6] in which AgOAc, $In(OAc)_3$, $Zn(OAc)_2$ and manganese stearate ($Mn(St)_2$) and thiourea precursors were thermally decomposed in the presence of a mixture of dodecanethiol (DDT) and OAm used as capping ligands. Green and orange-emitting AIZS QDs were prepared using Ag/In/Zn molar ratios of 0.02/0.02/0.16 and 0.06/0.06/0.08, respectively. The amount of DDT used to control the size of the nanocrystals was fixed at 2 mol% and the loading of $Mn(St)_2$ was varied (25, 50 or 75 mol% relative to the total amount of salts in the reaction medium). Further increasing the loading in $Mn(St)_2$ was found to be deleterious on the QDs optical properties (*vide infra*). In preliminary experiments, we observed that after complete dissolution of the precursors at room temperature, the optimal optical properties were obtained when heating the reaction mixture at 180°C and this temperature was kept in further experiments. The reaction mixture was maintained at 180°C for 10 min before cooling

to room temperature and purification of the QDs. Only weak shifts of the UV-visible absorption and of the PL emission to lower energy were observed during the 10 min of heating indicating that no significant growth of the nanocrystals occurred during that period.

Fig. 1 and S1 show X-ray diffraction (XRD) patterns of orange- and green-emitting AIZS and Mn:AIZS QDs, respectively. The broadness of the peaks is indicative of the small size of the nanocrystals. The peaks located at 25.4, 26.8, 28.8, 37.4, 44.9, 48.8 and 53.2° correspond to the (120), (002), (121), (122), (320), (123) and (322) planes of the AIS orthorhombic structure, respectively (JCPDS card No 25-1328, $Pna2_1$ space group, a = 0.7008 nm, b = 0.8162 nm and c = 0.6585 nm), as demonstrated by the Rietveld refinements using the Fundamental Parameters approach built in the Topas application (Bruker XAS) shown in Fig. S2. These results are in accordance with the synthetic method used.[6] The orthorhombic phase is stable above 620°C while the tetragonal chalcopyrite structure is stable below 620°C.[2] This phase reversion likely originates from the use of OAm as solvent which modifies the chemical growth environment of the nanocrystals.[2] The peaks are shifted towards larger angles compared to pure AIS crystals, due to the diffusion of Zn^{2+} and Mn^{2+} ions into the AIS core which conducts to a lattice shrinkage as the ion radii of Zn^{2+} (0.075 nm) and Mn^{2+} (0.070 nm) are smaller than that of In^{3+} (0.094 nm) and Ag^{+} (0.115 nm). No significant shift of XRD peaks was observed when varying the Mn^{2+} loading, indicating that Mn^{2+} ions were incorporated in the QDs without significant changes in their crystal structure. Finally, no impurity like Ag_2S, In_2S_3 or MnS was detected indicating that phase separation did not occur even using a high loading in Mn^{2+}.

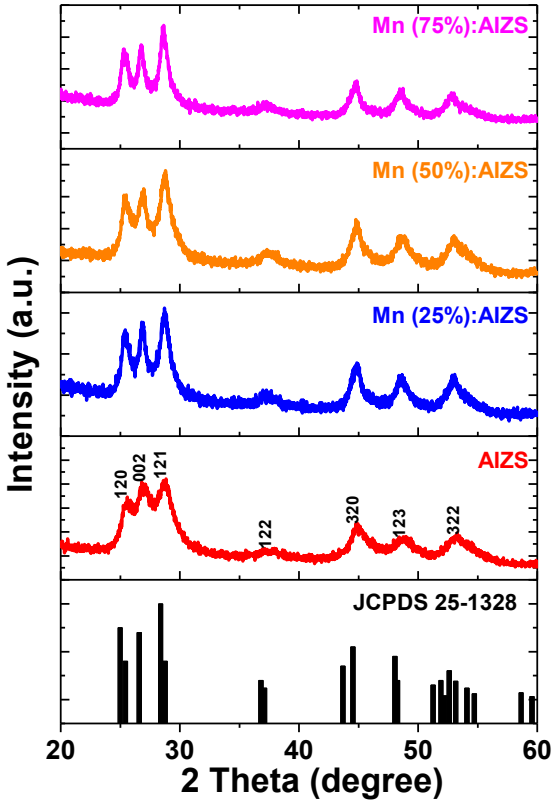

Fig. 1 XRD patterns of red-emitting AIZS and Mn:AIZS QDs when varying the Mn^{2+} loading.

Both energy-dispersive X-ray (EDX) and inductively coupled plasma-optical emission spectrometer (ICP-OES) analyses confirm the presence of Zn, Ag, In, Mn and S elements in Mn:AIZS QDs but the stoichiometry is different from that used for the synthesis (see Table 1 for ICP-OES results where the actual ratios of Ag/In/Mn/Zn are normalized to the molar amount of the Ag element and Fig. S3 and Table S1 for EDX results). According to EDX and ICP-OES analyses, the QDs have a non-stoichiometric composition with an excess of S compared to metal ions and a defect in Ag compared to In and Zn. The high amount of S detected originates from the presence of S both in the core and in the DDT capping ligand. While equimolar amounts of Ag and In were charged in the reaction flask, AIZS QDs obtained after purification appear significantly richer in the In element (In/Ag atomic ratio of 1.54). Although In^{3+} is a hard Lewis acid according to the Pearson theory while Ag^{+} and S^{2-} exhibit a soft character, this result may be related to the difference of chemical reactivity of Ag and In precursors towards S^{2-} in the reaction solution. When Mn^{2+} was loaded in the AIZS nanocrystals, the contents in Ag^{+} and In^{3+} of the QDs decrease while that of Zn^{2+} remains

almost constant, suggesting that a cation exchange allowing the replacement of Ag^{+} and In^{3+} by Mn^{2+} occurs. Finally, EDX analyses show that the amount of Mn^{2+} ions loaded in the nanocrystals is significantly lower that the amount used for the synthesis (1.82, 5.37 and 11.89 at.% of Mn^{2+} were detected when using 25, 50 and 75% of Mn^{2+} relative to the total amount of metallic salts used for the synthesis), suggesting that Mn^{2+} ions poorly incorporate into the AIZS crystal lattice.

Table 1. Theoretical and actual Ag/In/Mn/Zn ratios determined by ICP-OES for orange-emitting AIZS QDs when varying the Mn^{2+} loading

QDs	Ag/In/Mn/Zn ratio in precursors	Actual ratios of Ag/In/Mn/Zn
AIZS	1/1/0/1.33	1/1.54/0/1.80
Mn (25%):AIZS	1/1/0.83/1.33	1/1.55/0.17/1.97
Mn (50%):AIZS	1/1/1.66/1.33	1/1.62/0.55/2.02
Mn (75%):AIZS	1/1/2.5/1.33	1/1.47/1.44/2.38

Low temperature (20 K) X-band electron paramagnetic resonance (EPR) spectra recorded on the Mn:AIZS QDs further support the loading of Mn^{2+} in the nanocrystals. In all cases, a broad signal centered on g = 2 is detected. The broadness of the signal is typical for Mn-doped AIZS or CIZS QDs and originates from the complex environment of Mn^{2+} surrounded by Ag^{+}, In^{3+} and Zn^{2+} ions.[24] While poorly resolved hyperfine coupling can be observed for 50% and 75% loading in Mn^{2+}, the spectrum of the Mn (25%):AIZS QDs displays a set of six lines separated by about 80 G, which is related to the coupling of the electronic spin with the 5/2 nuclear spin of Mn^{2+}.

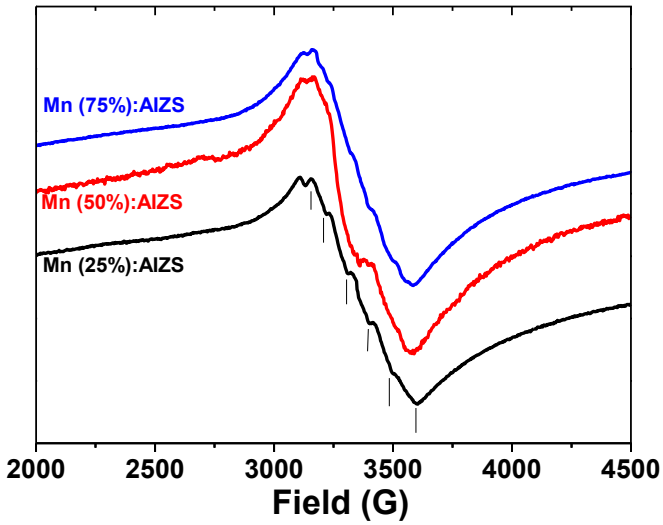

Fig. 2 EPR spectra recorded at 20 K of orange-emitting AIZS loaded with 25, 50 and 75% Mn^{2+}.

Transmission Electron Microscopy (TEM) and High-Resolution TEM (HR-TEM) were used to characterize the size and the shape of AIZS and Mn:AIZS QDs. Fig. 3 shows the results obtained with orange-emitting AIZS QDs when increasing the loading percentage in Mn^{2+} from 25 to 75%. The average size of the nanocrystals was determined by analyzing at least 100 nanocrystals in the TEM images and, regardless of the Mn-loading percentage, was found to vary between 3.3 and 3.7 nm (see Fig. S4 for the size distributions). Mn:AIZS QDs shape is irregular and spherical, ellipsoidal and triangular particles can be observed in each sample. The clear lattice fringes in the associated HR-TEM images confirm that Mn:AIZS QDs are single crystals. The lattice space measured is of ca. 0.35 nm and corresponds to the (120) crystal plane of orthorhombic $AgInS_2$. The high crystallinity of the dots is further evidenced from the selected area electron diffraction (SAED) patterns (insets of Fig. 3) which show a set of concentric rings corresponding to the diffraction of the various crystalline planes of the nanocrystals.

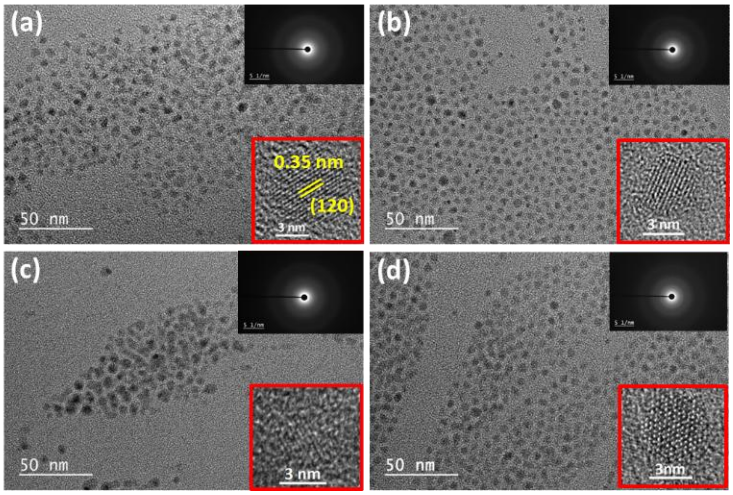

Fig. 3 TEM and HR-TEM images of (a) orange-emitting AIZS and (b-d) Mn:AIZS QDs loaded with 25, 50 and 75% Mn^{2+}, respectively. The insets shows SAED patterns.

A representative thermogravimetric analysis (TGA) of the Mn (50%):AIZS QDs is given in Fig. 4a and shows three mass loss regions. The two first mass losses (between 250-350°C and 360-460°C) likely originates from the removal of neutral ligand (DDT and OAm) anchored at the surface of the dots while the third weight loss might originate from the removal of ionic ligand (DDT covalently bound to surface Zn atoms). The remaining mass (ca. 73%) corresponds to the inorganic Mn:AIZS core and indicates that the QDs are covered by a relatively thick shell of ligands. The presence of the DTT and OAm ligands at the periphery of the dots was further confirmed by FT-IR. The symmetric and antisymmetric C-H stretching of methylene groups of OAm and DDT can be observed at 2916 and 2850 cm^{-1}, respectively, while the in-plane deformation of these bonds can be observed at 1453 cm^{-1}. The weak signal at 3002 cm^{-1} is characteristic of the ethylenic C-H stretching of OAm. The N-H stretching and bending appear at 3209 and 1614 cm^{-1}, respectively. The C-S stretching of DDT at 1375 cm^{-1} further confirms the co-capping of the dots with OAm and DDT.

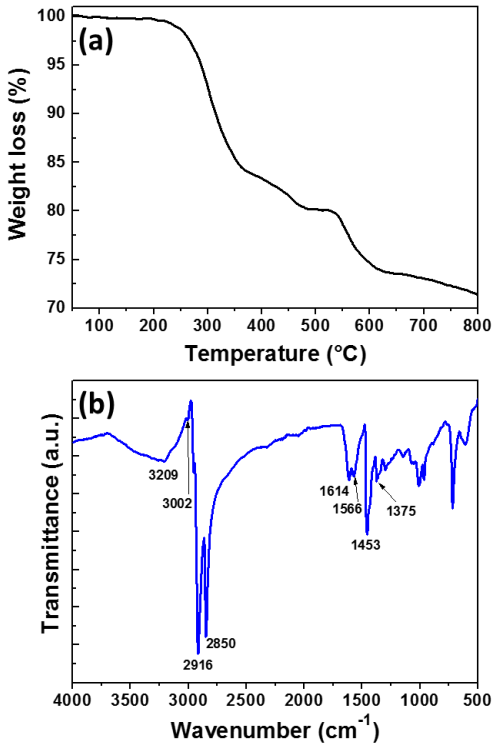

Fig. 4. (a) TGA trace and (b) FT-IR spectrum of Mn (50%):AIZS QDs.

Optical properties

Fig. 5 shows the UV-vis absorption and the PL emission spectra of green- and orange-emitting AIZS QDs and the evolution of these spectra when increasing the loading in Mn^{2+} from 25 to 75%. All spectra were recorded using nanocrystals obtained after 10 min heating at 180°C and purified by precipitation and washing with methanol. The broad absorption without a marked exciton band is typical of ternary like AIS and quaternary like AIZS QDs and originates from the distribution of vibrational states rather than from size and/or composition inhomogeneity of the dots.[1,2,28] A slight shift to lower energies is observed when increasing the loading in Mn^{2+}, which suggests a decrease of the bandgap and thus a modification of the electronic states of the AIZS core. The shift to lower energies may be caused by the lattice shrinkage originating from the diffusion of Mn^{2+} ions in the AIZS core as previously show by XRD experiments. The incorporation of Mn^{2+} ions in the AIZS core may also generate additional sub-bandgap transitions that may contribute to the tail absorption (vide infra). The bandgap values were determined from the Tauc plots of $(\alpha h\nu)^2$ vs hv (where α is the absorption coefficient and hv is the photon energy) and were found to

decrease from 2.52 to 2.31 and from 2.93 to 2.83 eV for orange- and green-emitting AIZS QDs, respectively, when loading these nanocrystals with 25, 50 and 75% Mn^{2+} (Fig. 6). These values are higher than that of bulk $AgInS_2$ in orthorhombic phase (1.87 eV) due to the quantum confinement effect in AIZS and Mn:AIZS QDs. The steady state PL emission spectra or green- and orange emitting AIZS QDs are broad and their fwhm are of ca. 100 and 138 nm, respectively (Fig. 5a-b). The maximum of the PL peaks are located at 540 and 660 nm and the PL QYs are 46 and 62% for the green and the orange-emitting QDs, respectively. As previously mentioned, the broadness and the asymmetry of the spectra originate from the numerous D-A transitions and trap-state emissions in these nanocrystals.[16-21] For both QDs, a marked Stokes shift is observed, indicating that the self-absorption is minimal and further corroborating that the PL emission is not a bandgap emission.

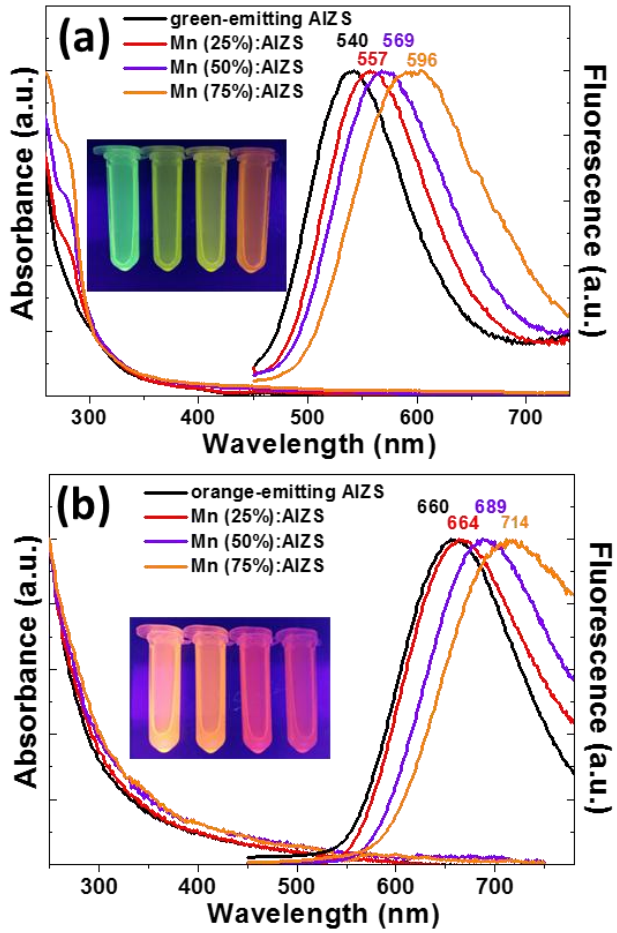

Fig. 5 UV-visible absorption and normalized PL emission spectra of (a) green and (b) orange emitting QDs when increasing the Mn^{2+} loading from 25 to 75% (λ_{ex} = 400 nm). The insets are digital photographs of the dots dispersed in chloroform under UV light illumination.

When loading these AIZS QDs with Mn^{2+}, a continuous red-shift from 540 to 596 nm and from 660 to 714 nm is observed compared to green- and orange-emitting QDs, respectively, indicating that Mn^{2+} ions contribute to the PL emission mechanism. However, contrary to previous reports describing the preparation of Mn-doped AIZS QDs, the $^4T_1 \rightarrow {}^6A_1$ emission of Mn^{2+} ions in the AIZS host was not observed at ca. 600 nm, which suggest that Mn^{2+} ions incorporated in AIZS QDs via the synthetic method developed in this work do not quench the D-A pair emission.[24,25] PL excitation (PLE) spectra of AIZS and Mn (25%):AIZS QDs are shown in Fig. S5. A broad signal with a maximum located at ca. 520 nm was observed for both QDs, which is in good agreement with previously described PLE spectra of AIZS QDs emitting in red region.[13,19] PLE have been also measured (not shown here) for an emission from 550 nm to 900 nm with a step equal to 4 nm for AIZS and Mn:AIZS and the spectra show the same shape. The similar profiles confirm that the Mn^{2+}-related $^4T_1 \rightarrow {}^6A_1$ transition is not involved in the PL excitation and emission of Mn:AIZS QDs. We assume that the PL red-shift observed when increasing the dopant loading likely originates from the Mn^{2+} position in the AIZS host and thus from the synthetic method used.

The PL shifts do not originate from a size increase of the dots as indicated by TEM (Fig. 3 and S4) but rather from a decrease of the bandgap as previously demonstrated. Simultaneously, their shape was also found to be dependent on the Mn^{2+} loading and the fwhm of the PL peak increases up to 144 and 170 nm for Mn:AIZS QDs emitting at 596 and 714 nm, respectively, while it should be of ca. 60 nm for the Mn d-state emission.[24] The PL intensity of Mn:AIZS QDs remains high but a continuous decrease of the PL QY is observed when increasing the Mn^{2+} content. For green-emitting AIZS, the PL QY decreases from 46 to 38, 31 and 13% for theoretical loadings in Mn^{2+} of 25, 50 and 75%. A similar behavior is observed starting from orange-emitting QDs (decrease from 62 to 53, 41 and 16%, respectively).

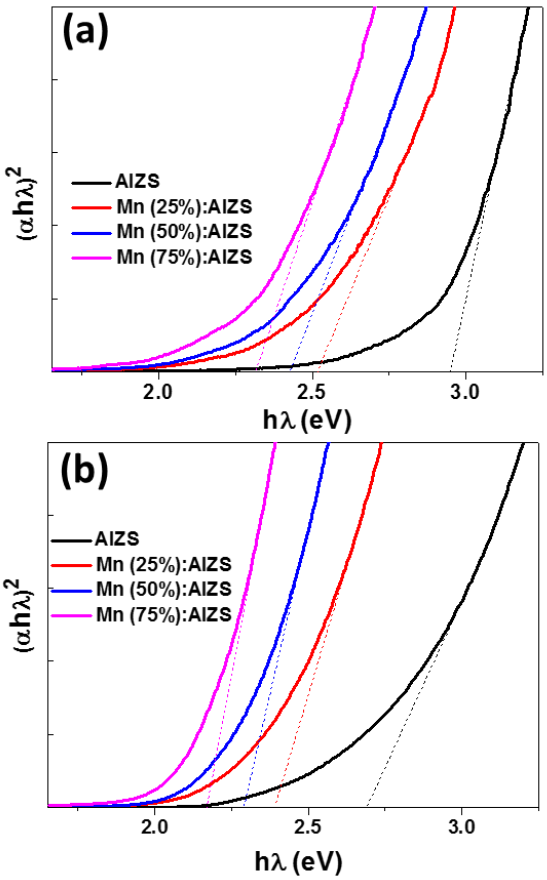

Fig. 6 Determination of the optical bandgap of AIZS and Mn:AIZS QDs when increasing the loading in Mn^{2+} ions in (a) green-emitting AIZS QDs and (b) orange-emitting AIZS QDs.

The PL mechanism for AIZS QDs is presented schematically in Fig. 7a and shows the radiative D-A pair recombination. On the basis of the previously described results, the position of the trap state A relative to the Mn^{2+} $^6A_1$ state determines the recombination process.[16-21,24] If the trap state A is located below the Mn^{2+} $^6A_1$ state, the typical $^4T_1 \rightarrow {}^6A_1$ transition of Mn^{2+} yielding an orange PL at ca. 600 nm should be observed (Fig. 7b).[24] The dependence of the PL emission peak with the Mn^{2+} content suggests that a new Mn^{2+} dependent trap state located above the $^6A_1$ state and with a gradually higher energy appears while increasing the Mn^{2+} loading of AIZS QDs as demonstrated by the continuous red-shift of the PL peak with the increase of the Mn^{2+} content (Fig. 7c).

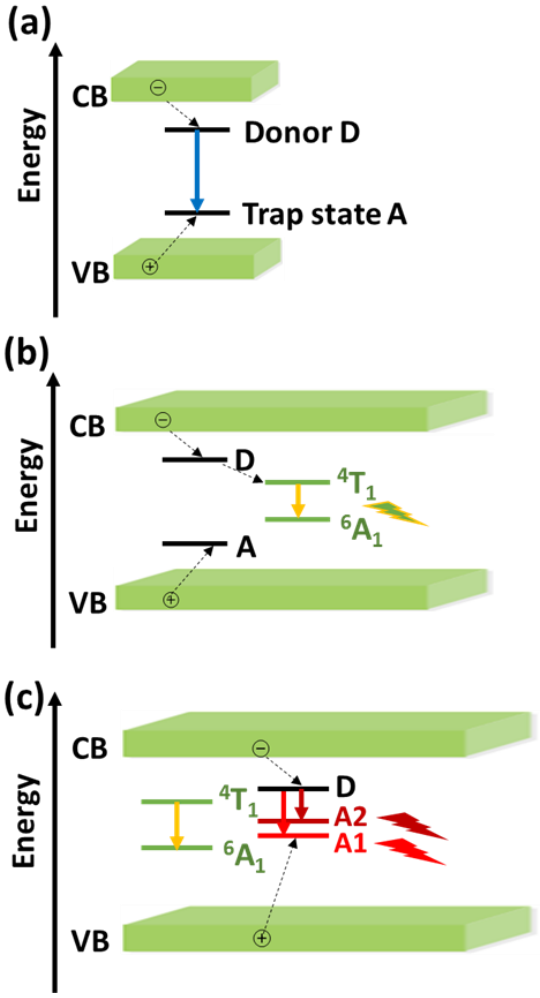

Fig. 7 Schematic illustration of the PL mechanism of (a) AIZS and (b-c) Mn:AIZS QDs. The solid arrows correspond to radiative relations while the dotted arrows show the non-radiative relaxations.

To further study the mechanism of the PL emission, time-resolved PL decay measurements were carried out. Representative time-resolved PL decay spectra were recorded at the PL emission maxima of orange-emitting AIZS and Mn:AIZS QDs obtained from Fig. 5a and results are shown in Fig. 8. The data were best fitted using a bi-exponential function $I(t) = A_1 \exp(-t/\tau_1)$ and $A_2 \exp(-t/\tau_2)$ where τ_1 and τ_2 are the time constants of the PL and A_1 and A_2 the normalized amplitudes of the components. The fitting parameters are summarized in Table 2. The average PL lifetimes (τ_{av}) were determined using $\tau_{av} = (A_1\tau_1 + A_2\tau_2)/(A_1 + A_2)$ and are in the typical range of 1 to 10 μs^{-1} generally observed for AIZS nanocrystals due to the numerous intrinsic trap states (V_S and Ag_{int} acting as donors while V_{Ag} and S_{int} as acceptors).[11,16-21,29] These results

further confirm that the PL emission does not originate from Mn^{2+} ions which exhibits a millisecond PL lifetime.[30,31]

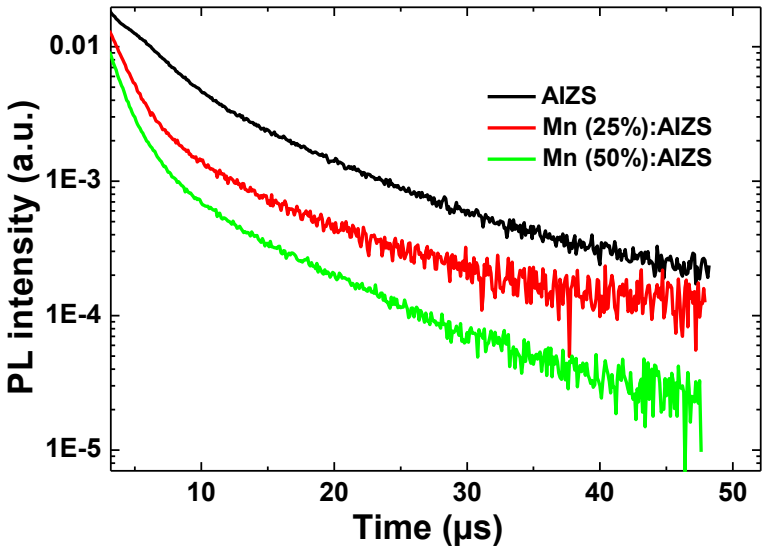

Fig. 8 PL lifetimes of orange-emitting AIZS and of the corresponding Mn:AIZS QDs at the PL maximum wavelength.

Table 2 Lifetimes and fitting parameters of orange-emitting AIZS and Mn:AIZS nanocrystals

Sample	A_1 (%)	τ_1 (µs)	A_2 (%)	τ_2 (µs)	τ_{av} (µs)
AIZS	54.1	2.738	45.9	10.143	6.14
Mn (25%):AIZS	75.8	1.471	24.2	8.146	3.09
Mn (50%):AIZS	87.8	1.344	12.2	7.832	2.14

These long PL lifetimes clearly differentiate AIZS QDs from binary QDs like CdSe or CdTe that exhibit a short PL lifetime of tens of nanoseconds originating from band to band emission.[32] As previously described, two radiative channels were observed.[33] The fast decay component τ_1 corresponds to surface trap state recombination and the slow decay component τ_2 to the D-A recombination originating from the defect states within the bandgap. Until 50% loading in Mn^{2+}, which corresponds to the dots with a PL QY only weakly affected by the Mn^{2+} incorporation (*vide supra*), a decrease of the

decay time of both components is observed. This decrease is however more pronounced for the fast component, suggesting a more pronounced influence of Mn^{2+} ions on the surface-related states. Moreover, its amplitude A_1 increases, indicating that the observed evolution of the time-resolved PL can be interpreted by the promotion of energy migration from Mn^{2+} to the surface quench centers as observed in previous studies.[27]

Magnetic properties

AIZS QDs do not display any magnetic response with the applied field. When Mn^{2+} is incorporated within the nanocrystals, and regardless of the loading percentage, the magnetic moment (*M*) is the merge of a ferromagnetic signal (evident from the hysteresis at low fields in the inset of Fig. 9b,d and f) and of a paramagnetic and/or superparamagnetic signal (evident from the overall Langevin-like shape of the curves at high fields). Previous works demonstrated that nanocrystals doped with Mn^{2+} display a ferromagnetic behavior[34-38] whereas the Mn^{2+} ions are well known to be paramagnetic.[39,40] The coercivity H_c (the applied field required for zero net moment) and the remanence M_r (the magnetic moment at zero applied field) can both be trivially extracted from the hysteresis loops (Fig. 9b and d). The samples synthesized at high concentration of Mn^{2+} exhibit the highest saturation magnetization, up to 0.25 emu/g (at 10 K) (Fig. 9a), and decrease above 0.02 emu/g at room temperature. The decrease of the amount of Mn^{2+} leads to the decrease of Ms values below 0.17 emu/g, and the temperature dependence is drastically increased. All Mn:AIZS QDs exhibit remanent magnetization (Fig. 9a and c), up to 0.001 emu/g at 10 K. Fig. 9e depicts the behavior of the Mn (25%):AIZS doped sample, no influence of the temperature on the magnetic behavior of the QDs can be evidenced. The extraction of saturation magnetization (M_s) from the curves is non-trivial, since saturation was not achieved in the system due to persisting paramagnetic signal on top of the ferromagnetic signal of interest.

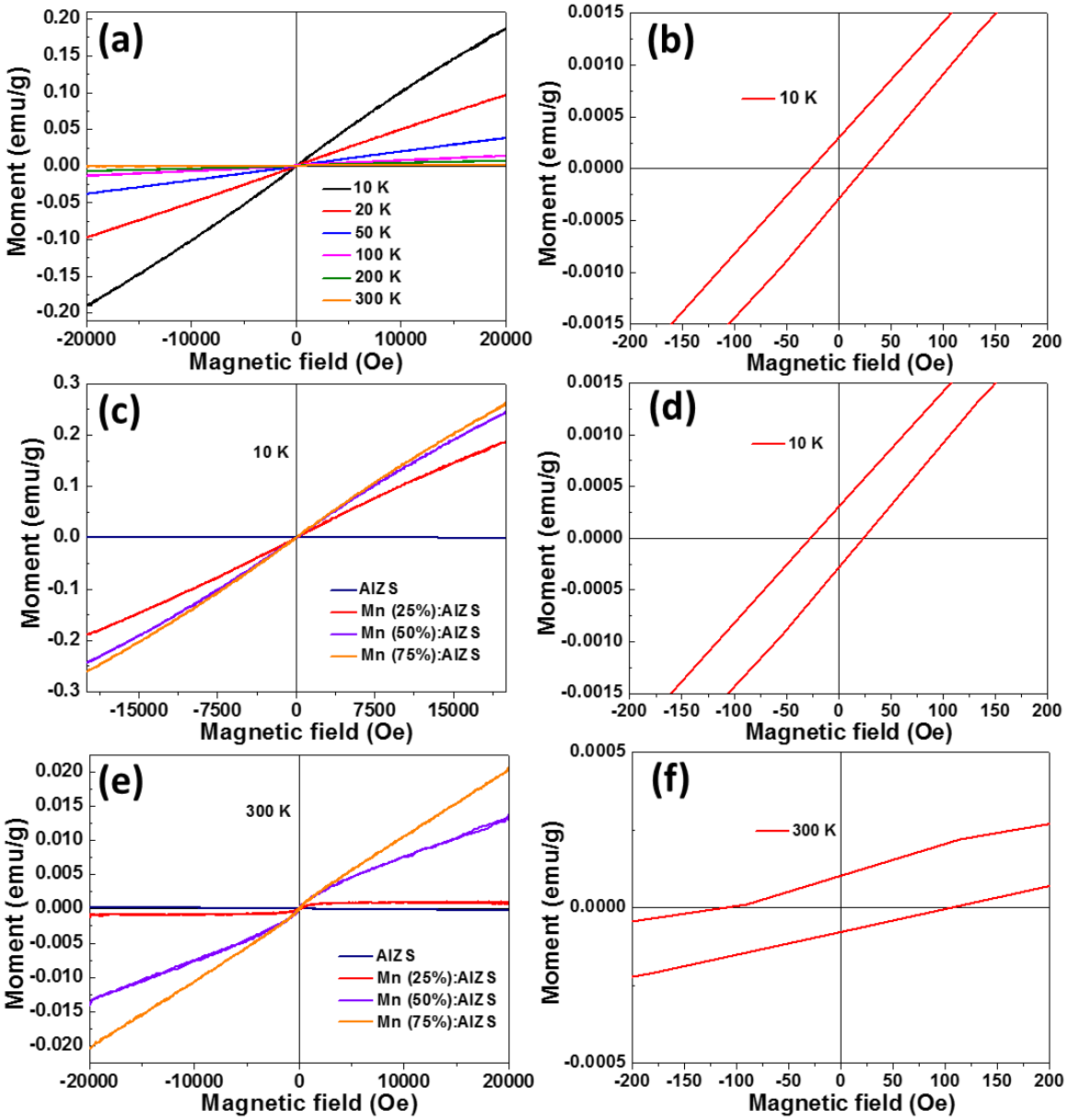

Fig. 9. (a) M(H) loop curves of Mn (25%):AIZS QDs at different temperatures and (b) the magnetic properties at zero field. (c) and (e) are the M(H) loop curves of AIZS and Mn:AIZS QDs at 10K and 300K, respectively. (d) and (f) describe the magnetic properties at zero field.

Transfer of Mn:AIZS QDs in aqueous phase

To demonstrate the potential of Mn:AIZS QDs for biological applications, the DDT and OAm-capped Mn:AIZS QDs were transferred into aqueous phase using the amphiphilic PMAO polymer.[12] Micelles were first produced by the association of the hydrophobic alkyl chains of PMAO with those of DDT and OAm through self-assembly

in chloroform. After evaporation of the solvent, maleic anhydride units were hydrolyzed into carboxylate functions. This hydrophilic corona allows the successful transfer of Mn:AIZS QDs in water without alteration of their optical properties. Empty micelles were removed by ultracentrifugation at 15000 rpm and the PMAO-encapsulated Mn:AIZS QDs can easily be dispersed in water, PBS or borate buffer. These colloidal dispersions can be stored for months at 4°C indicating the high stability of the micelles. Except for the Mn (75%):AIZS QDs, a red-shift of the PL emission is observed but the PL QYs were not significantly altered (59, 51, 40 and 11% for AIZS and Mn:AIZS loaded with 25, 50 and 75% Mn^{2+}, respectively) (Fig. 10). The red-shift observed likely originates from the compact association of QDs in the core of the micelle in which the light emitted by the smallest nanocrystals is adsorbed by the largest ones that emit a higher wavelength like a Förster resonance energy transfer process.[41,42]

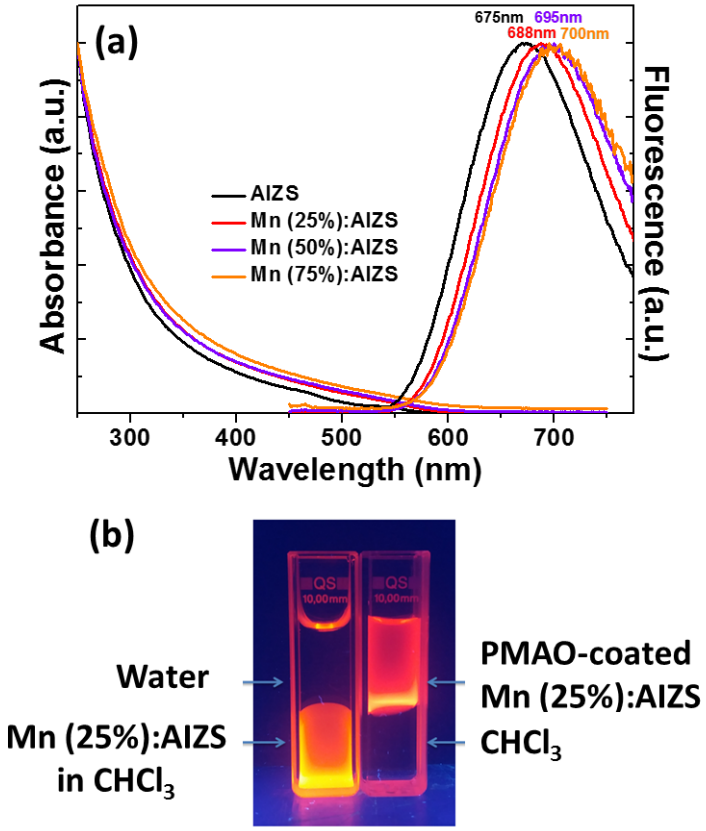

Fig. 10. (a) UV-visible and PL emission spectra of AIZS and Mn:AIZS QDs after transfer in water using the PMAO polymer and (b) digital photograph taken under UV light illumination of Mn (25%):AIZS QDs before and after their transfer into water.

Conclusions

In summary, Mn:AIZS QDs were easily prepared via a one-step approach using AgOAc, $In(OAc)_3$, $Zn(OAc)_2$, $Mn(St)_2$ and thiourea as precursors DDT and OAm as capping ligands. The PL emission of Mn:AIZS originates from D-A transitions and can easily be tuned by varying the Ag/In/Zn/Mn stoichiometric ratio. A red-shift of the PL emission is observed when increasing the Mn^{2+} loading likely due to the generation of Mn^{2+} dependent trap states. Mn:AIZS QDs were also demonstrated to exhibit ferromagnetic and paramagnetic properties. Their long PL lifetimes, which allow to differentiate their signals from the fast decaying background and biological systems PL, and their magnetic properties should allow Mn:AIZS QDs to be of high potential for bioimaging applications.

Experimental

Materials

Silver acetate (≥99.0%, Sigma-Aldrich), indium acetate (99.99%, Sigma-Aldrich), zinc acetate dihydrate (≥98%, Sigma-Aldrich), thiourea (≥99.0%, Sigma-Aldrich), oleylamine (OAm, technical grade, 70%, Aldrich), 1-dodecanethiol (DDT, 98%, Alfa Aesar), stearic acid (SA, 97%, Acros organics), methanol (≥99.9%, Carlo Erba Reagents), manganese chloride tetrahydrate (≥99.0%, Sigma), tetramethylammonium hydroxide pentahydrate (TMAH, ≥97%, Sigma), poly(maleic anhydride-alt-1-octadecene) (PMAO, 30.000-50.000, Sigma-Aldrich), and chloroform (≥99%, Carlo Erba Reagents) were used as received.

Synthesis of Mn(+2) stearate ($MnSt_2$)

Under a nitrogen atmosphere, stearic acid (10 mmol) in 15 mL of methanol was heated to 50-60°C to make a homogeneous solution. After cooling the reaction mixture to room temperature, TMAH (10 mmol) in 20 mL of methanol was added and the mixture was further stirred 15 min. Next, $MnCl_2{\cdot}4H_2O$ (5 mmol) in 10 mL of methanol was added dropwise under vigorous stirring. The white $MnSt_2$ precipitate was collected by centrifugation, washed several times with methanol and dried under vacuum. The dried $MnSt_2$ was stored at 4°C under N_2 before use.

Synthesis of $(AgInS_2)_x(ZnS)_{1-x}$ (AIZS) and $(AgInS_2)_x(MnS)_y(ZnS)_{1-x-y}$ (Mn:AIZS) QDs

$(AgInS_2)_x(ZnS)_{1-x}$ (AIZS) and $(AgInS_2)_x(MnS)_y(ZnS)_{1-x-y}$ (Mn:AIZS) QDs were prepared according to a facile one-step method recently described [6], with slight modifications. Green emitting nanocrystals were prepared by heating 0.02 mmol of AgOAc, 0.02 mmol of $In(OAc)_3$, 0.16 mmol of $Zn(OAc)_2$ and 0.2 mmol of thiourea in 3 mL of OAm containing 2 mol% of DDT. Red emitting nanocrystals were prepared by heating 0.06 mmol of AgOAc, 0.06 mmol of $In(OAc)_3$, 0.08 mmol of $Zn(OAc)_2$ and 0.2 mmol of thiourea in 3 mL of OAm containing 2 mol% of DDT. The $Mn(St)_2$ loading was varied (25, 50 or 75 mol% relative to the total amount of salts used). The precursors and ligands were mixed in a four-necked flask and the mixture stirred under an argon atmosphere until dissolution. Next, the temperature was increased to 180°C and maintained for 10 min. The reaction mixture was then cooled to room temperature and centrifuged to remove large aggregates. AIZS or Mn:AIZS QDs were precipitated from the supernatant using methanol and further purified by washing with methanol and centrifugation (at least 10 times). The nanocrystals were dried under vacuum at room temperature and stored in a dark place for further characterizations.

Hydro-dispersion of AIZS@DDT QDs with PMAO

To disperse Mn:AIZS@DDT QDs in water, the amphiphilic polymer poly(maleic-alt-1-octadecene) (PMAO) was used [12]. A mixture of Mn:AIZS@DDT QDs (6 mg), PMAO

(9.4 mg) and 10 mL of chloroform was stirred vigorously for 2h at ambient temperature. Next, the solvent was removed at room temperature by using a rotary evaporator. The obtained product was dissolved in 1 mL of chloroform and 6 mL of a 0.05 M aqueous solution of NaOH were added. This mixture was sonicated for 1 h at 50°C and next centrifuged for 15 min at 5000 rpm to remove aggregates. Next, the supernatant was centrifuged for 30 min at 15000 rpm and the pellet obtained was dispersed in a Borate Buffer solution (pH = 9) and stored at 4°C.

Characterization

TEM and HR-TEM images were taken by placing a drop of the particles in water onto an ultrathin carbon film-supported gold grids. XRD studies were carried out by using an X'Pert MPD diffractometer (Panalytical AXS). The samples were placed on zero background quartz sample holders and the XRD patterns were recorded at room temperature using Cu K_α radiation (λ = 0.15418 nm). A Jeol ARM 200F microscope equipped with EDX spectrometry was used for the energy-dispersive X-ray (EDX) analysis. The actual compositions of Mn:AIZS QDs was also determined using an inductively coupled plasma-optical emission spectrometer (ICP-OES) (Thermo). The samples were prepared by digestion of the dried QDs with HCl/HNO_3 3:1 (v/v) for 12 h, followed by dilution with Milli-Q water. TGA was conducted under O_2 atmosphere from room temperature to 800°C at a heating rate of 10°C/min using a TGA/DSC1 STAR equipment (Mettler-Toledo). X-band EPR spectra were recorded in non-saturating conditions on a Bruker ELEXSYS 500 spectrometer equipped with an Oxford instrument continuous-flow liquid-helium cryostat and a temperature control system. Typical conditions were : 5G amplitude modulation, 9.402GHz, microwave power : 2.52 mW.

All the optical measurements were performed at room temperature (20 ± 1°C) under ambient conditions. FT-IR spectra were recorded on a Bruker ALPHA spectrometer. Absorption spectra were obtained with a Thermo Scientific Evolution 220 UV-visible spectrophotometer, while PL spectra were measured on a Horiba Fluoromax-4 Jobin Yvon spectrofluorimeter. PL spectra were spectrally corrected and PL QYs were determined relative to Rhodamine 6G in ethanol (PL QY = 94%). For the PL excitation

measurements, a Horiba Jobin Yvon Fluorolog spectrofluorimeter equipped with a Xe lamp source was used. The PL signal was analyzed by a monochromator equipped with a 150 grooves/mm grating and by a CCD detector cooled at 200 K. For the time resolved photoluminescence (TR- PL) experiments, the QDs were pumped by the 355 nm line of a frequency-tripled YAG (yttrium aluminium garnet):Nd laser. The laser pulse frequency, energy and duration were typically equal to 10 Hz, 50 μJ and 10 ns, respectively. The PL signal was analyzed by a monochromator equipped with a 600 grooves/mm grating and by a photomultiplier tube cooled at 190 K. The rise time of the detector is equal to around 3 ns.

Magnetic properties were characterized with vibrating sample magnetometry (VSM) at temperatures of 10 and 300 K, with applied magnetic field (*H*) up to ± 9 T. The magnetic moment values are reported in electromagnetic units (emu) per mass unit of sample.

Conflicts of interest

There are no conflicts to declare.

Acknowledgements

The authors thank the Bolashak International Scholarship of JSC "Center for International Programs" for financial support.

Notes and references

1 H. Zhong, Z. Bai and B. Zou, *J. Phys. Chem. Lett*., 2012, **3**, 3167-3175.

2 D. Wang, W. Zheng, C. Hao, Q. Peng and Y. Li, *Chem. Commun.,* 2008, 2556-2558.

3 S. Liu and X. Su, *RSC Adv.,* 2014, **4**, 43415-43428.

4 G. Xu, S. Zeng, B. Zhang, M. T. Swihart, K. -T. Yong and P. N. Prasad, *Chem. Rev*., 2016, **116**, 12234-12327.

5 W. M. Girma, M. Z. Fahmi, A. Parmadi, M. A. Abati and J. -Y. Chang, *J. Mater. Chem. B*, 2017, **5**, 6193-6216.

6 T. Kameyama, T. Takahashi, T. Machida, Y. Kamiya, T. Yamamoto, S. Kuwabata and T. Torimoto, *J. Phys. Chem. C*, 2015, **119**, 24740-24749.

7 H. Abdullah and D. -H. Huo, *ACS Appl. Mater. Interfaces*, 2015, **7**, 26941-26951.

8 D.B. Choi, S. Kim, H.C. Yoon, M. Ko, H. Yang and Y. R. Do, *J. Mater. Chem. C*, 2017, **5**, 953-959.

9 R. Boonsin, A. Barros, F. Donat, D. Boyer, G. Chadeyron, R. Schneider, P. Boutinaud and R. Mahiou, *ACS Photonics*, 2018, **5**, 462-470.

10 M. Jagadeeswaravao, A. Swarnkar, G. B. Markad and A. Nag, *J. Phys. Chem. C*, 2016, **120**, 19461-19469.

11 J. Song, C. Ma, W. Zhang, S. Yang, S. Wang, L. Lv, L. Zhu, R. Xia and X. Xu, *J. Mater. Chem. B*, 2016, **4**, 7909-7918.

12 M. Michalska, A. Florczak, H. Dams-Kozlowska, J. Gapinski, S. Jurga and R. Schneider, *Acta Biomater.*, 2016, **35**, 293-304.

13 W. -W. Xiong, G. -H. Yang, X. -C. Wu and J. -J. Zhu, *J. Mater. Chem. B*, 2013, **1**, 4160-4165.

14 H. Shinchi, M. Wakao, N. Nagata, M. Sakamoto, E. Mochizuki, T. Hematou, S. Kuwabata and Y. Suda, *Bioconjugate Chem.,* 2014, **25**, 286-295.

15 L. Wang, X. Kang and D. Pan, *Inorg. Chem*., 2017, **56**, 6122-6130.

16 B. Mao, C. -H. Chuang, J. Wang and C. Burda, *J. Phys. Chem. C*, 2011, **115**, 8945-8954.

17 Y. Hamanaka, T. Ogawa and M. Tsuzuki, *J. Phys. Chem. C*, 2011, **115**, 1786-1792.

18 M. J. Rao, T. Shibata, S. Chattopadhyay and A. Nag, *J. Phys. Chem. Lett*., 2014, **5**, 167-173.

19 B. Mao, C. -H. Chuang, C. McCleese, J. Zhu and C. Burda, *J. Phys. Chem. C*, 2014, **118**, 13883-13889.

20 S. Jeong, H. C. Yoon, N. S. Han, J. H. Oh, S. M. Park, B. K. Min, Y. R. Do and J. K. Song, *J. Phys. Chem. C*, 2017, **121**, 3149-3155.

21 O. Stroyuk, A. Raevskaya, F. Spranger, O. Selyshchev, V. Dzhagan, S. Schulze, D. R. T. Zahn and A. Eychmüller, *J. Phys. Chem. C*, 2018, **122**, 13648-13658.

22 K. Hattori, K. Akamatou and N. Kamegashira, *J. Appl. Phys.*, 1992, **71**, 3414-3418.

23 S. H. You, K. J. Hong, C. J. Youn, T. S. Jeong, J. D. Moon, H. S. Kim and J. S. Park, *J. Appl. Phys*., 2001, **90**, 3894-3898.

24 G. Manna, S. Jana, R. Bose and N. Pradhan, *J. Phys. Chem. Lett*., 2012, **3**, 2528-2534.

25 X. Tang, Z. Zu, L. Bian, J. Du, W. Chen, X. Zeng, M. Wen, Z. Zang and J. Xue, *Mater. Des*., 2016, **91**, 256-261.

26 P. Zhou, X. Zhang, L. Li, X. Liu, L. Yuan and X. Zhang, *Opt. Mater. Express*, 2015, **5**, 2069-2080.

27 B. Huang, Q. Dai, N. Zhuo, Q. Jiang, F. Shi, H. Wang, H. Zhang, C. Liao, Y. Cui and J. Zhang, *J. Appl. Phys*., 2014, **116**, 094303.

28 T. Takahashi, A. Kudo, S. Kuwabata, A. Ishikawa, H. Ishihara, Y. Tsuboi and T. Torimoto, *J. Phys. Chem. C*, 2013, **117**, 2511-2520.

29 M. Dai, S. Ogawa, T. Kameyama, K. -I. Okazaki, A. Kudo, S. Kuwabata, Y. Tsuboi and T. Torimoto, *J. Mater. Chem*., 2012, **22**, 12851-12858.

30 A. Aboulaich, M. Geszke, L. Balan, J. Ghanbaja, G. Medjahdi and R. Schneider, *Inorg. Chem.*, 2010, **49**, 10940-10948.

31 R. Zhou, S. Sun, C. Li, L. Wu, X. Hou and P. Wu, *ACS Appl. Mater. Interfaces*, 2018, **10**, 34060-34067.

32 F. Aldeek, L. Balan, G. Medjahdi, T. Roques-Carmes, J. -P. Malval, C. Mustin, J. Ghanbaja and R. Schneider, *J. Phys. Chem. C*, 2009, **113**, 19458-19467.

33 X. S. Tang, W. B. A. Ho and J. M. Xue, *J. Phys. Chem. C*, 2012, **116**, 9769-9773.

34 A. Albert manoharan, R. Chandramohan, R. David prabu, S. Valanarasu, V. Ganesh, Mohd Shkir, A. Kathalingam and S. AlFaify, *J. Mol. Struct*., 2018, **1171**, 388-395.

35 S. Ravi and F. Winfred Shashikanth, *Mater. Lett*., 2015, **141**, 132-134.

36 Sh. Zhu, Ch. Chen, Zh. Li, *J. Magn. Magn. Mater*., 2019, **471**, 370-380.

37 N. Sharma, A. Gaur and R.K. Kotnala, *J. Magn. Magn. Mater*., 2015, **377**, 183-189.

38 Ch. Jing, Y. Jiang, W. Bai, J. Chu and A. Liu, *J. Magn. Magn. Mater*., 2010, **322**, 2395-2400.

39 R. Zhou, Sh. -K. Sun, Ch. Li, L. Wu, X. Hou and P. Wu, *ACS Appl. Mater. Interfaces*, 2018, **10**, 34060-34067.

40 J. Amighian, E. Karimzadeh and M. Mozaffari, *J. Magn. Magn. Mater*., 2013, **332**, 157-162.

41 M. Booth, R. Peel, R. Partanen, N. Hondow, V. Vasilia, L. J. C. Jeuken and K. Critchley, *RSC Adv*., 2013, **3**, 20559-20566.

42 S. Chen, M. Ahmadiantehrani, N. G. Publicover, K. W. Hunter and X. Zhu, *RSC Adv*., 2015, **5**, 60612-60620.